ACS Catalysis

pubs.acs.org/acscatalysis Research Article

Rapid Hole Extraction Based on Cascade Band Alignment Boosts Photoelectrochemical Water Oxidation Efficiency

Fushuang Niu, Quan Zhou, Yiming Han, Rong Liu, Zijian Zhao, Zhenghao Zhang, and Ke Hu*

Cite This: *ACS Catal.* 2022, 12, 10028−10038 Read Online

ACCESS | Metrics & More | Article Recommendations | Supporting Information

ABSTRACT: Photon energy loss to interfacial charge recombination is one of the key challenges to achieving high efficiencies for solar water splitting in photoelectrochemical cells (PECs). Herein, $BiVO_4$-based photoanodes are constructed, where $BiVO_4$, cadmium sulfide nanosheets (CdS NSs), hole transport molecules (HTs), and oxygen evolution cocatalysts (OECs) assemble sequentially in a cascade band alignment for efficient photogenerated hole extraction and accumulation to OECs. In the photoanode assemblies, CdS NSs act as energetic barriers to suppress surface recombination. Thiolate-functionalized aryl amine HTs that anchor to CdS NSs are interfacial-charge-transfer mediators that efficiently extract the photogenerated holes. The oxidized HT (HT^+) hops isoenergetically among adjacent HTs and finally accumulates oxidative equivalents to OEC. Transient absorption spectroscopy along with intensity-modulated photocurrent spectroscopy proves that HTs and CdS NSs accelerate hole-transfer kinetics and suppress recombination of surface-accumulated holes and electrons. Among the three HTs, triphenylamine shows the best performance. The best-performing photoanode assembly exhibits increased photocurrent density from 0.87 to 5.2 mA/cm^2. The molecular approach to hole extraction from $BiVO_4$ photoanodes provides a promising avenue for efficient photogenerated charge separation and collection to optimize the performance of PEC for water splitting.

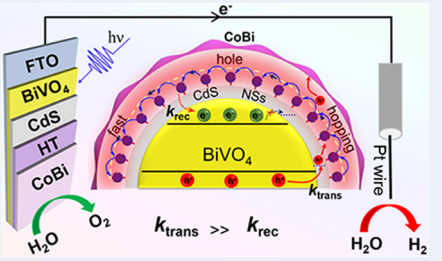

KEYWORDS: *$BiVO_4$ photoanode, hole transport molecules, hole transfer, transient absorption spectroscopy, photoelectrochemical water splitting*

INTRODUCTION

Water splitting using photoelectrochemical cells (PECs) is an environmentally friendly and sustainable way to convert solar energy into chemical energy.[1−3] $BiVO_4$ (BVO) has been considered one of the most promising photoanode materials due to its suitable band gap (2.4−2.5 eV)[4] and deep valence band edge, which enable visible-light harvesting and water oxidation.[5−8] Unfortunately, BVO has a short hole diffusion length of only 70 nm and thereby suffers from rapid charge recombination[9] at the surface/electrolyte interface,[10,11] which limits BVO's water oxidation efficiency in PEC cells.

Recently, a great deal of effort has been devoted to overcoming short hole diffusion length and rapid charge recombination of BVO photoanodes, through heteroatom doping,[12−14] oxygen vacancies[15] or structural tuning,[7] heterostructure construction,[16] and loading of oxygen evolution cocatalysts (OECs).[17] Loading OEC on a BVO surface is regarded as a feasible approach to optimize PEC activity.[1,18−21] However, severe electron−hole recombination at the BVO/OEC interface still limits the PEC water oxidation. It is crucial to exploit a novel electron−hole separation channel between BVO and OEC. Hole extraction layer (HEL) is one of the most effective approaches to boost PEC performance.[22−24] Rapid hole extraction can not only effectively suppress charge recombination but also improve the small thermodynamic water oxidation driving force.[25] For example, p-type black phosphorus,[5] graphene quantum dots,[26] ultrathin g-C_3N_4 layers,[27] porphyrins-Co,[2] polyaniline,[28] and covalent triazine-based polymers[29] as HELs were inserted between BVO and OEC. These HELs were found to help extract holes from photoexcited BVO and boost PEC performance. However, most hole extraction materials, especially polymer-based, are relatively difficult to disperse uniformly on the BVO surface and they lack flexibility of tuning redox potentials to optimize the interfacial band alignment. To the best of our knowledge, there has so far been no report about the uniform molecular monolayer as the typical HEL on the BVO-based photoanode. Small molecules based on aryl amine compounds have shown fast hole transport kinetics.[30−36] Besides, synthetic control of molecular hole transport molecules enables fine-tuning of redox potentials. If the redox potential of HT is too positive, hole extraction may not have enough driving force. The opposite also holds true for the hole accumulation to the cocatalyst.

Received: June 8, 2022
Revised: July 19, 2022
Published: August 3, 2022

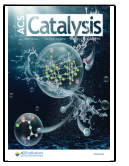

Scheme 1. (A, B) Fabrication of the BVO|CdS-HT|CoBi Photoanode and the Photogenerated Carrier Transfer Process. (C) Molecular Structures of Three HTs (CZ, TPA, PTZ)

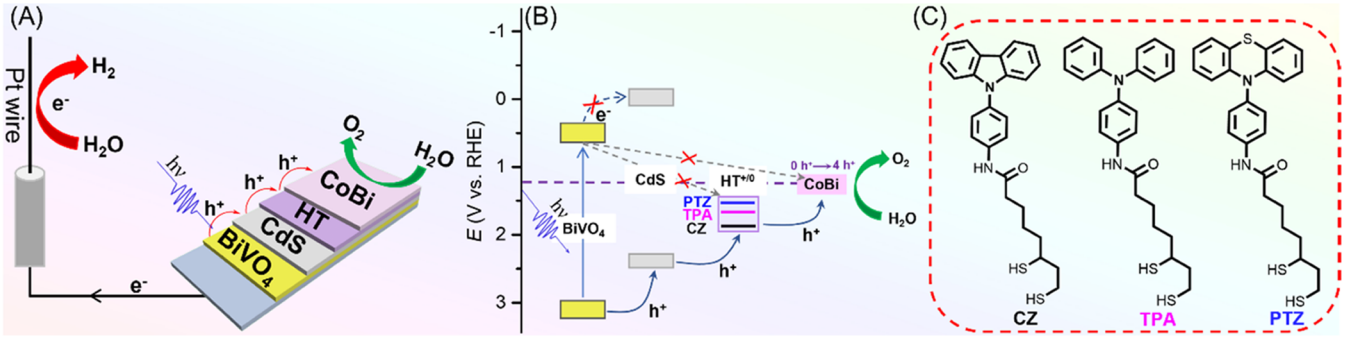

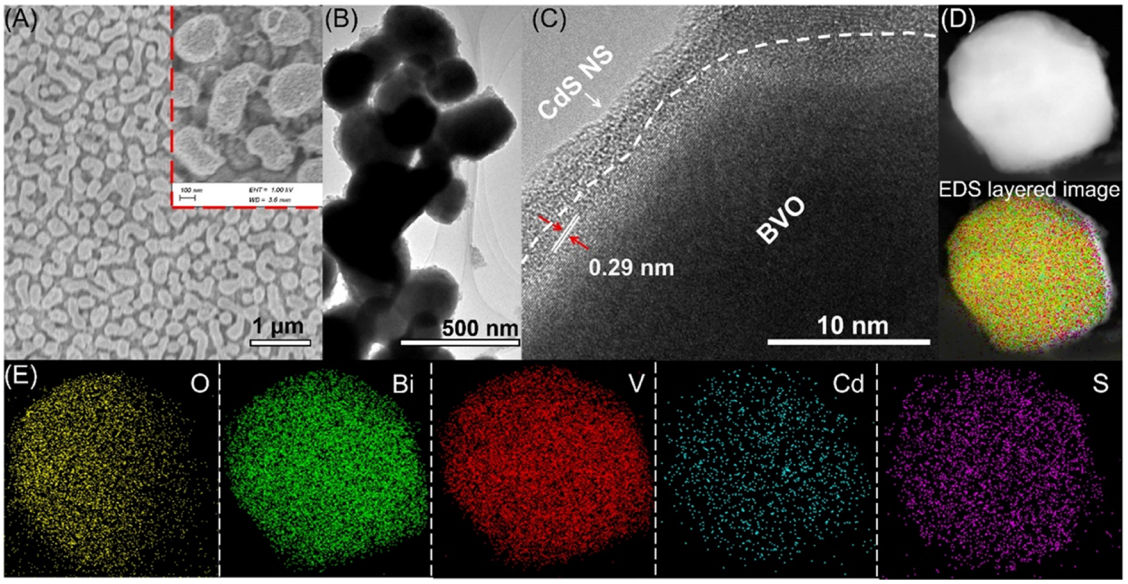

Figure 1. Morphology and composition characterization of BVO|CdS. (A) Scanning electron microscopy (SEM) (inset is the zoom-in SEM image), (B) transmission electron microscopy (TEM), and (C) high-resolution TEM (HRTEM) of the BVO|CdS photoanode. (D) TEM image and energy-dispersive X-ray spectrum (EDS) layered image. (E) EDS for O, Bi, V, Cd, and S elements.

After careful consideration of both thermodynamics and the hole mobility of hole extraction materials, we developed a strategy for facilitating the kinetics of hole extraction of BVO-based photoanodes for boosting PEC water splitting. The general design principle is shown in Scheme 1A. A thin layer of cadmium sulfide nanosheets (CdS NSs) is grown on the surface of BVO. The use of the CdS NS overlayer on BVO (denoted as BVO|CdS) is threefold: (1) to form a heterojunction with BVO to extract holes from photogenerated electron−hole pairs in bulk BVO; (2) to provide a surface suitable for dithiolate anchoring to form a molecular monolayer; and (3) to act as an energetic barrier for charge recombination between BVO(e^-) and HT^+. A series of hole transport molecules (HTs) including carbazole, triphenylamine, and phenothiazine derivatives (denoted as CZ, TPA, and PTZ, respectively) with tunable energy band alignments were constructed further onto BVO|CdS. HTs were uniformly anchored onto the surface of CdS NSs to form a molecular monolayer through dithiolate groups, as described in our previous paper.[37] Photogenerated holes are rapidly extracted by HTs with an appropriate thermodynamic driving force. Then, the oxidized HT, HT^+ hops isoenergetically among adjacent HTs and finally accumulates oxidative equivalents to OEC. Finally, the outer surface is coated with a thin layer of OEC (CoBi). The photogenerated holes are strongly driven from BVO to the outer CoBi surface by the cascade band alignment of the heterostructure for efficient water oxidation. Transient absorption spectroscopy and intensity-modulated photocurrent spectroscopy characterizations prove that the layer of HT-anchored CdS NSs that are sandwiched between BVO and OECs greatly enhances the kinetics of interfacial hole transfer (52 times higher than that of pristine BVO) and effectively suppresses recombination of surface-accumulated holes with BVO conduction band electrons, thereby significantly improving the performance of PEC water oxidation.

RESULTS AND DISCUSSION

Design and Synthesis of the Photoanodes. As shown in Scheme 1, we designed a rational and feasible strategy with the aim of suppressing the recombination of accumulated holes with electrons at the interface by improving the kinetics of charge transfer upon light excitation. The photoanode was integrated as follows. First, the mesoporous BVO films were grown on the fluorine-doped SnO_2 (FTO) substrates through a previously reported method (see the Experimental Section

https://doi.org/10.1021/acscatal.2c02773
ACS Catal. 2022, 12, 10028−10038

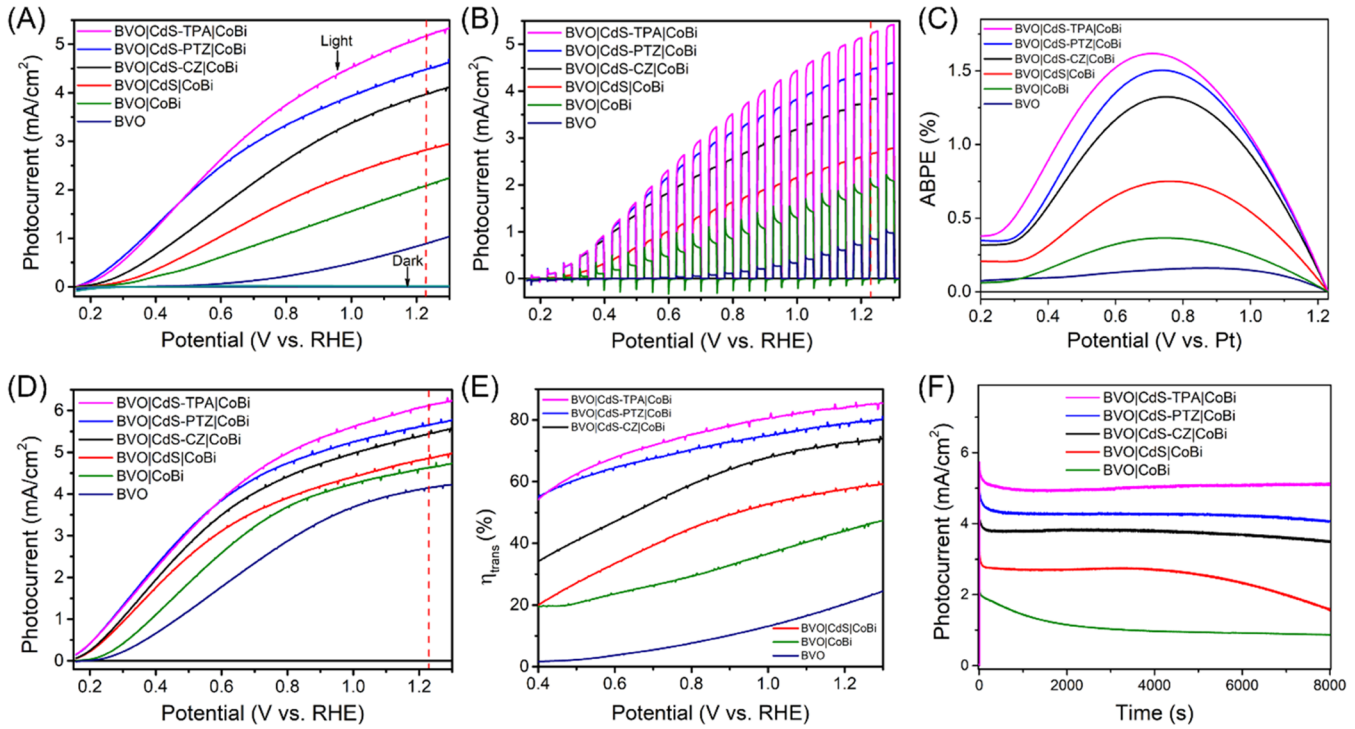

Figure 2. Photoelectrochemical water oxidation activity of integrated photoanodes as well as control samples. (A) Photocurrent density vs applied potential curves of different integrated photoanodes at a scan rate of 10 mV/s. (B) Photocurrent density vs applied potential curves of different integrated photoanodes under chopped visible-light illumination. (C) ABPE curves of different integrated photoanodes obtained using a two-electrode cell for PEC water splitting. (D) Photocurrent density vs applied potential curves of different integrated photoanode with the hole scavenger Na_2SO_3 at a scan rate of 10 mV/s. (E) Charge transfer efficiency curves of different integrated photoanodes. (F) Stability test of different integrated photoanodes at a potential of 1.2 V vs RHE under visible-light illumination. All measurements were performed in 0.5 M potassium borate buffer electrolyte (pH 9.3) under visible-light (400 nm long pass cut filter, 100 mW/cm^2) back-illumination.

for details).[38] Second, CdS NSs coated on the BVO films were synthesized by chemical bath deposition (denoted as BVO|CdS). Then, the HTs were anchored onto BVO|CdS by immersing the BVO|CdS films in 50 mM HT loading solutions overnight (denoted as BVO|CdS-HT). The surface coverages of HTs on the BVO|CdS films were determined using the Beer−Lambert law in which the absorption decreases of the loading solutions were probed at 310 nm for TPA, 320 nm for PTZ, and 294 nm for CZ, before and after immersion of the BVO|CdS films (Figure S1; see the Experimental Section for details). The surface coverages of TPA, PTZ, and CZ on BVO|CdS were approximately the same (~$1.8 \pm 0.2 \times 10^{-8}$ mol/cm^2). The about the same surface coverages are attributed to the similar molecular footprints as well as the identical dithiolate anchoring groups. Finally, cobalt borate (CoBi), as a widely used OEC, was deposited on BVO|CdS-HT via *a* photoassisted electrodeposition method to enhance PEC activity (denoted as BVO|CdS-HT|CoBi).

The absorption increase from UV to blue-light regions in UV−vis diffuse reflectance spectroscopy (DRS; see Figure S2) suggested that the CdS NSs were successfully grown on the surface of BVO. Scanning electron microscopy (SEM) images of the as-prepared BVO|CdS films (Figure 1A) showed that the BVO|CdS films were uniformly grown on FTO substrates. The high-resolution SEM shown in the inset of Figure 1A indicated that the BVO|CdS sample was composed of interconnected nanoparticles with sizes ranging from 200 to 300 nm. A uniform CdS NS overlayer coated on the surface of BVO was observed from transmission electron microscopy (TEM); Figure 1B. The thickness of CdS NSs was about 3 nm according to the high-resolution TEM; Figure 1C. Note that the lattice fringe of 0.29 nm was indexed to the (040) plane of BVO.[1,2,38] TEM-EDS mapping (Figure 1D,E) was used to analyze the overall distribution of CdS NSs on the BVO surface, which further confirmed that the CdS NSs were uniformly coated on the BVO surface. Unlike the bare BVO surface that prohibited molecular anchoring from most of the common anchoring groups such as carboxylates or phosphonates,[39] the CdS NS overlayer provided thiolate anchoring sites for molecular monolayer adsorption.

PEC Performances of Integrated Photoanodes. To evaluate the water oxidation performance of different integrated photoanodes, PEC measurements were conducted in a three-electrode cell with 0.5 M potassium borate buffer solution as the electrolyte under 100 mW/cm^2 visible-light (with a 400 nm long pass filter) illumination. Figure 2A displays the PEC performances of different integrated photoanodes. The BVO photoanode alone showed a low photocurrent, 0.87 mA/cm^2 at 1.23 V versus (vs) the reversible hydrogen electrode (RHE). As expected, the CoBi catalyst resulted in an enhancement in the photocurrent and an improvement in the onset potential by 153 mV compared with the pristine BVO (355 mV vs RHE). When the thin CdS NSs were introduced between BVO and CoBi, the BVO|CdS|CoBi photoanodes showed a much higher photocurrent (2.67 mA/cm^2) than that of the BVO (0.87 mA/cm^2) or BVO|CoBi (1.98 mA/cm^2) photoanode. This was attributed to the CdS NSs filling the BVO surface state and suppressing surface recombination by creating a solid-state heterojunction, which was beneficial for charge transfer.[40] More strikingly, after the

https://doi.org/10.1021/acscatal.2c02773
ACS Catal. 2022, 12, 10028−10038

Scheme 2. (A, B) Diagram of the Integrated Photoanodes and Photogenerated Carrier Transfer without CdS-HT and with CdS-HT. (C) Simplified Interfacial Electron Transfer and Hole Hopping Scheme of the BVO|CdS-HT|CoBi Photoanode for Solar Water Oxidation

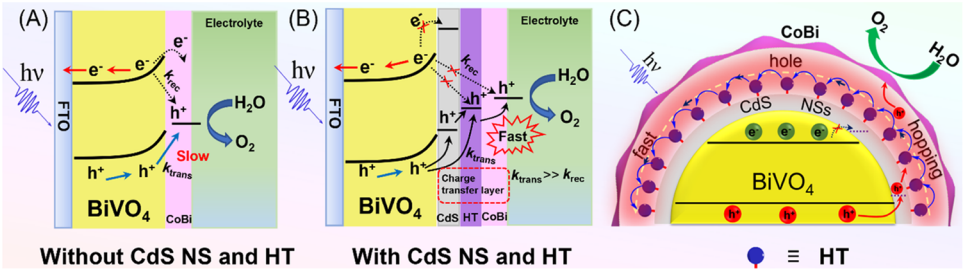

HTs were anchored onto the CdS NSs, the integrated photoanodes, including BVO|CdS-TPA|CoBi, BVO|CdS-PTZ|CoBi, and BVO|CdS-CZ|CoBi, all showed superior performance as compared to BVO|CdS|CoBi. Among all of the integrated photoanodes, BVO|CdS-TPA|CoBi showed the highest photocurrent density of 5.2 mA/cm^2, with an ultralow onset potential of 0.15 V vs RHE. The $HT^{+/0}$ redox potential follows the order: E^0 ($CZ^{+/0}$)> E^0 ($TPA^{+/0}$)> E^0 ($PTZ^{+/0}$). We speculate that the redox potential of TPA had the best energetic and kinetic balance between hole extraction from CdS and hole transfer to CoBi, so TPA has the best performance compared to other HTs.

Figure 2B shows the photocurrent density vs applied potential response of the different integrated photoanodes under chopped visible-light illumination. The BVO|CoBi photoanode showed evident transient anodic current spikes at the moments of the light being turned on, suggesting that surface charge recombination is still a major energy loss process. The enlargement of Figure 2B is shown in Figure S3. When the light was turned off, the evident transient current spikes below zero were also observed, indicating interfacial back-electron transfer to oxidized CoBi. This was the major reason for the poor performance of PEC water oxidation in the BVO|CoBi photoanode, as shown in Scheme 2A. More interestingly, once the CdS NSs and HTs were inserted between the BVO and CoBi, no transient cathodic/anodic current spike at the time of dark/light switches was observed (Figure S3), indicating that CdS NSs and HTs greatly suppressed the recombination of surface-accumulated holes with back electrons, as shown in Scheme 2B.

For the BVO|CoBi photoanode, some photogenerated holes participated in turning over water to oxygen, whereas a large quantity just recombined with the electrons, resulting in the low OER activity (Scheme 2A). However, the BVO|CdS-HT|CoBi photoanode where CZ, TPA, and PTZ anchoring on CdS NSs was introduced showed superior PEC performance. The BVO|CdS solid-state heterojunction facilitated the transfer of photogenerated holes to the HTs and suppressed the recombination between HT^+ and BVO conduction band electrons, as shown in Scheme 2B. HT^+ hopped isoenergetically among adjacent HTs and finally accumulated oxidative equivalents to CoBi for water oxidation, as shown in Scheme 2C. It is clear that the introduction of HTs that uniformly anchored on CdS NSs could enhance the separation and transfer of the photogenerated charges, thereby significantly improving the PEC performance. To achieve the true photoelectrode efficiency, applied bias photo-to-current efficiencies (ABPEs) of different integrated photoanodes were calculated as shown in Figure 2C based on the *J-V* curve measured in a two-electrode configuration against Pt (Figure S4). Remarkably, the excellent ABPE of the BVO|CdS-TPA|CoBi photoanode reached 1.63% at 0.70 V vs Pt (calculated by eq S1), which was about 10 times higher than that of BVO alone (0.158%).

To quantify the improvement of surface-electrolyte hole-transfer kinetics, photocurrent density vs applied potential curves of different integrated photoanodes were measured in 0.5 M potassium borate electrolyte with 0.2 M Na_2SO_3 as the hole scavenger, as shown in Figure 2D. The charge transfer efficiency (η_{trans}) of the different integrated photoanodes was calculated by eq S2 (see the Experimental Section for details). The value of η_{trans} was calculated according to the photocurrent density with and without the Na_2SO_3 hole scavenger (Figure 2E). The η_{trans} of the BVO photoanode was only ~21.5% at 1.23 V vs RHE; both the CdS NSs and CoBi coated on the BVO surface could effectively improve the surface hole-transfer efficiency. Notably, when HTs were anchored onto the CdS NSs to form BVO|CdS-HT|CoBi, the η_{trans} was further improved to 84.4% at 1.23 V vs RHE, which was 3.93 times that of pristine BVO. In summary, both CdS NSs and HTs highly improved the surface-electrolyte hole transfer to enhance the performance of PEC water oxidation.

Figure 2F shows the long-term stability of different integrated photoanodes over hours. The BVO|CdS-HT|CoBi photoanodes showed higher stability than that of BVO|CoBi and BVO|CdS|CoBi photoanodes. The photocurrent density response of the BVO|CoBi photoanode decayed rapidly to a low level presumably due to sluggish water oxidation kinetics and the instability of BVO. It is worth noting that a stable photocurrent density at 1.20 V vs RHE was obtained for the BVO|CdS|CoBi photoanode for 1 h, but then it started to decrease gradually. We speculate that although CdS NSs were able to suppress the surface charge recombination, they still had sluggish kinetics of water oxidation due to the slow kinetics of hole transfer to CoBi. Therefore, the CdS NSs were gradually corroded by the photogenerated holes.[41] As a result, the photocurrent density decreases gradually. On the contrary, BVO|CdS-HT|CoBi retained a stable photocurrent density at 1.20 V vs RHE. The uniform anchoring of HTs on the CdS NSs enhanced the kinetics of charge transfer to CoBi, which led to fast water oxidation reaction on the CoBi catalyst and efficient utilization of holes. Consequently, the CdS NSs were protected from the corrosion of photogenerated holes, which improved the stability of BVO|CdS-HT|CoBi photoanode PEC water oxidation.

To elucidate the oxygen evolution reaction (OER) of the integrated photoanode and the hydrogen evolution reaction (HER) of the counter electrode Pt wire in this PEC system,

https://doi.org/10.1021/acscatal.2c02773
ACS Catal. 2022, 12, 10028−10038

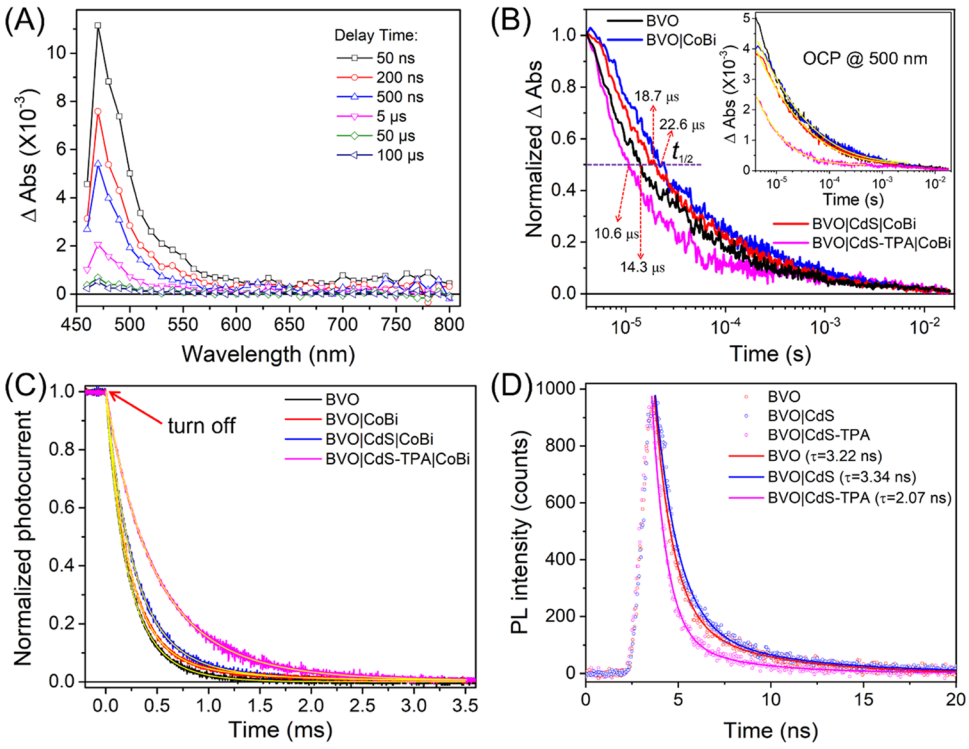

Figure 3. Transient absorption (TA) spectroscopy of different integrated photoanodes in 0.5 M potassium borate buffer solution excited by pulsed 355 nm laser excitation (0.6 mJ/cm^2 per pulse). (A) TA of FTO|BVO thin films as a function of indicated delay times after pulsed 355 nm laser excitation. (B) Normalized time-resolved trace monitored at 500 nm at OCP; inset: time-resolved kinetic traces monitored at 500 nm under OCP, and overlaid in yellow are KWW fits. (C) Transient photocurrent for different integrated BVO-based photoanodes; overlaid in yellow are biexponential function fits. (D) Time-resolved photoluminescence (TRPL) spectra of BVO, BVO|CdS, and BVO|CdS-TPA (excitation: λ = 400 nm).

the oxygen and hydrogen productions were quantified by gas chromatography (GC). The corresponding H_2 and O_2 evolutions were measured by GC every 2000 s. The produced H_2 and O_2 of the BVO|CdS-TPA|CoBi photoanode were 176.1 and 87.9 μmol/cm^2 after 8000 s, respectively, corresponding to the stoichiometric ratio of 2:1 for water splitting, as shown in Figure S5. It is found that the faradic efficiency (calculated by FE (%) = (96485 × $n(O_2)$ × 4)/Q) values of OER and HER are close to 99%. However, O_2 produced from the BVO|CdS|CoBi photoanode was 40.2 μmol/cm^2, while H_2 produced from the Pt counter electrode was 98.5 μmol/cm^2 after 8000 s, with an FE of 78.3%. Through the above discussion, although all three HTs (CZ, TPA, and PTZ) brought an enhancement in PEC water oxidation performance, TPA anchored onto the CdS NS-integrated photoanode showed the best performance, which offered the model for the following discussion.

Light-Driven Interfacial Charge Separation in the Photoanode. Data from photocurrents as well as FE of OER and HER measurements clearly indicated the advantage of HT for boosting BVO-based PEC water splitting. Nanosecond transient absorption measurements were used to investigate the electron transfer processes from the impact of HTs that were uniformly anchored on CdS NSs in the series of integrated photoanodes. As shown in Figure 3A, TA spectra of the pristine BVO thin film at indicated time delays were recorded after pulsed laser excitation at 355 nm (0.6 mJ/cm^2 per pulse) and the TA signal of surface-trapped holes for BVO mainly appeared from 460 to 700 nm, consistent with a prior report.[42] The transient absorption peak at 500 nm was chosen to monitor the BVO hole concentration kinetics for different integrated photoanodes under open-circuit potential (OCP) in 0.5 M potassium borate buffer solution (pH 9.3). The TA of the pristine BVO photoanode showed a shorter decay half-time ($t_{1/2}$ = 14.3 μs) relative to the BVO|CoBi photoanode ($t_{1/2}$ = 22.6 μs), indicating that the CoBi layer could passivate the BVO surface trap state and partly suppress the charge recombination, as shown in Figure 3B.[18] Inserting CdS NSs between BVO and CoBi decreased the hole lifetime ($t_{1/2}$ = 18.7 μs), which suggested that the formation of BVO and CdS NS heterostructures could promote hole transfer. Notably, the decay half-time of the TPA-introduced BVO|CdS-TPA|CoBi photoanode was only 10.6 μs, which was shorter than that of the BVO|CdS|CoBi photoanode ($t_{1/2}$ = 18.7 μs). The results indicated that TPA as HT facilitated the extraction of photogenerated holes, fast hopping, and accumulation to OEC (CoBi) instead of dwelling inside BVO, as illustrated in Scheme 2C. From the inset of Figure 3B, introducing the CoBi catalyst and CdS NSs resulted in a decrease in the initial TA intensity compared to that of BVO, which can be ascribed to the CoBi and CdS NSs accelerating the kinetics of hole transfer. Adding TPA further decreased the initial TA intensity due to the lower yield of BVO(h^+) on the surface of BVO. This proved that TPA serving as HT played an important role in promoting the hole extraction and further hole accumulation to the CoBi with sufficient hole-transfer driving forces. For the BVO|CdS-TPA|CoBi and BVO|CoBi photoanodes, pulsed laser excitation of the BVO resulted in photogenerated holes (BVO(h^+)) being extracted to the surface-attached TPA or CoBi and the hole-transfer process can be described in eqs 1−3.

https://doi.org/10.1021/acscatal.2c02773
ACS Catal. 2022, 12, 10028−10038

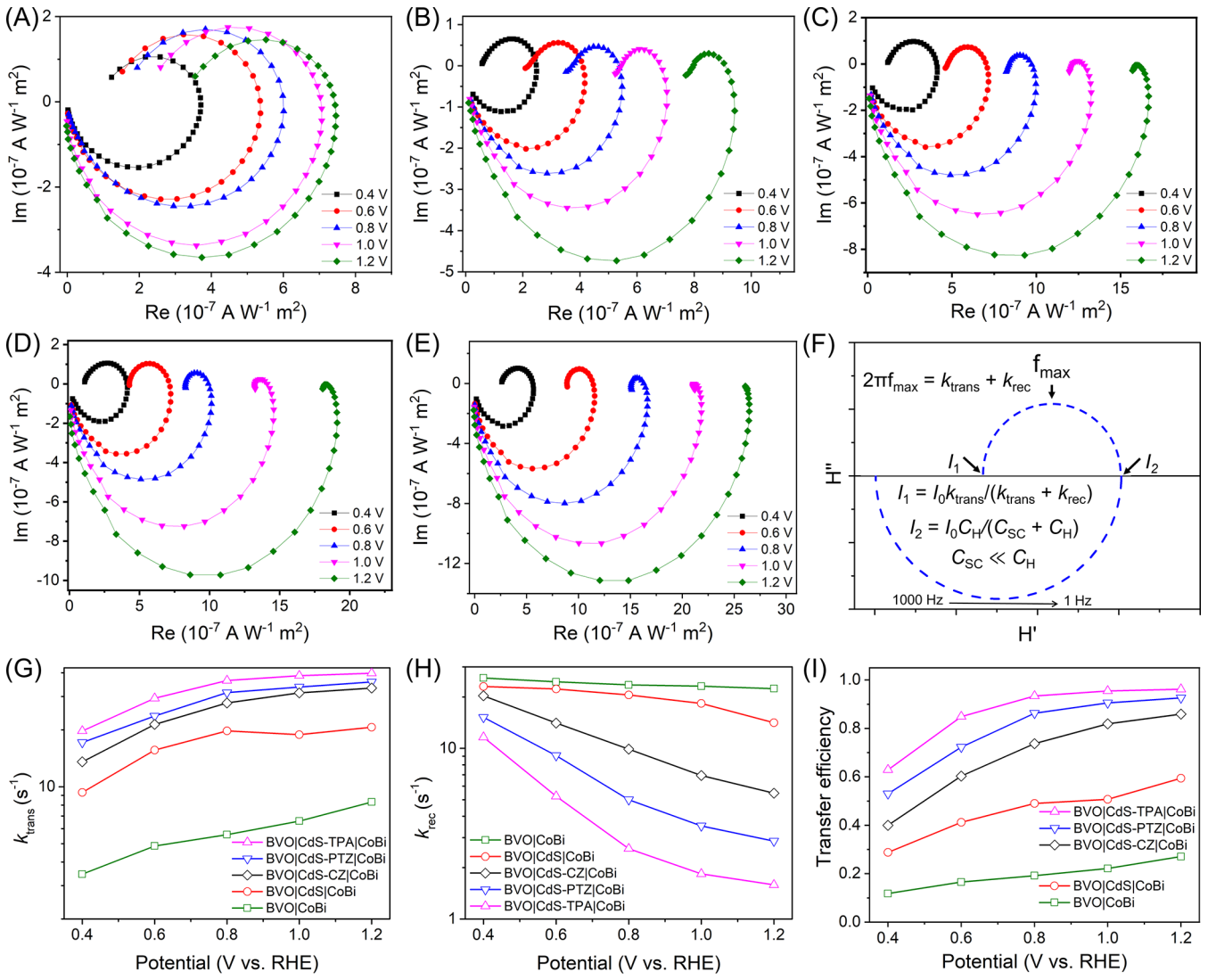

Figure 4. IMPS responses of (A) $BiVO_4$|CoBi, (B) $BiVO_4$|CdS|CoBi, (C) $BiVO_4$|CdS-CZ|CoBi, (D) $BiVO_4$|CdS-PTZ|CoBi, and (E) $BiVO_4$|CdS-TPA|CoBi photoanodes at various applied potentials. (F) Calculated example of the IMPS spectrum; various properties (e.g., charge transfer rate constant, surface recombination rate constant) can be obtained based on the multiple points of such a spectrum. (G) Rate constant for charge transfer (k_{trans}), (H) rate constant for charge recombination (k_{rec}), and (I) charge transfer efficiency extracted from the IMPS spectra of different photoanodes at various potentials.

$$\mathrm{BVO(e^-, h^+)|CoBi} \xrightarrow{k_{ht}} \mathrm{BVO(e^-)|CoBi(h^+)} \quad (1)$$

$$\mathrm{BVO(e^-, h^+)|CdS-TPA|CoBi} \xrightarrow{k'_{ht}} \mathrm{BVO(e^-)|CdS-TPA(h^+)|CoBi} \quad (2)$$

$$\mathrm{BVO(e^-)|CdS-TPA(h^+)|CoBi} \xrightarrow{k''_{ht}} \mathrm{BVO(e^-)|CdS-TPA|CoBi(h^+)} \quad (3)$$

Quantitative hole-transfer kinetics (k_{ht}) can be obtained using the Kohlrausch–Williams–Watts (KWW) function (eq 4), where β is inversely related to the width of the underlying Lévy distribution of the rate constants, A_0 the initial absorbance, and k is the characteristic observed rate constant. The average hole-transfer rate constant calculated based on eq 5,[43] $\overline{k_{ht}}$ of BVO(h^+) to TPA (3.9×10^6 s^{-1}) was about 52 times that of BVO(h^+) to CoBi (7.5×10^4 s^{-1}).

$$\Delta\mathrm{Abs} = A_0 \exp[-(kt)^{\beta}] \quad (4)$$

$$\overline{k_{ht}} = \left[\frac{1}{k\beta} \times \Gamma\left(\frac{1}{\beta}\right)\right]^{-1} \quad (5)$$

Transient photocurrent (TPC) measurements were also performed for different integrated BVO-based photoanodes, as shown in Figure 3C, which could directly reveal the lifetimes of the trapped holes and the hole separation and recombination efficiency.[44−46] The TPC signals were characterized in terms of two time constants (τ_1 and τ_2) and corresponding probability constants (φ_1 and φ_2), as listed in Table S1. The average decay time (τ) of the pristine BVO photoanode (0.27 ms) was shorter than that of the BVO|CoBi photoanode (0.39 ms) and that of the BVO|CdS|CoBi photoanode (0.40 ms) at 1.23 V vs RHE. However, the average decay times (τ) of the BVO|CdS-TPA|CoBi photoanode was 0.56 ms, about 2.1 times that of the pristine BVO photoanode. The results from TPC measurements further proved that TPA anchoring on CdS NSs indeed improved the hole lifetime and retarded electron–hole pair recombination for the BVO|CdS-TPA|CoBi photo-

https://doi.org/10.1021/acscatal.2c02773
ACS Catal. 2022, 12, 10028−10038

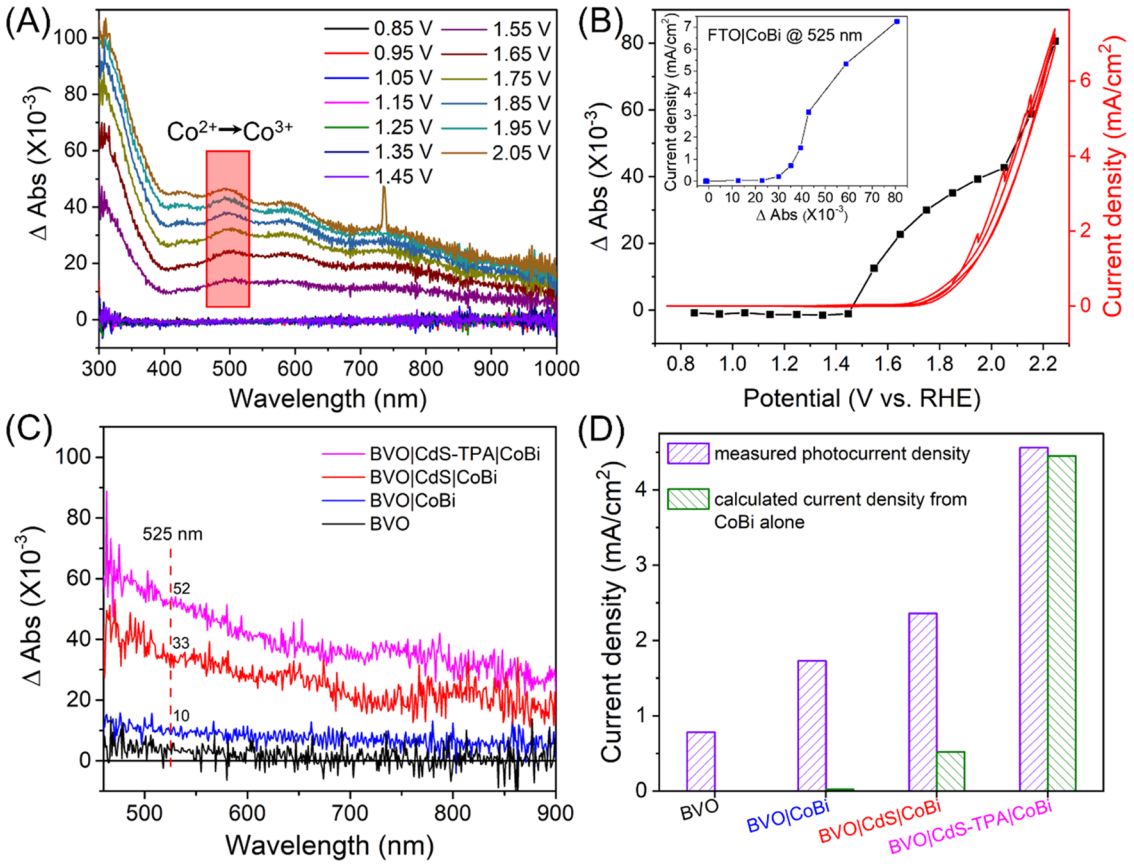

Figure 5. (A) SEC difference spectra of FTO|CoBi measured as a function of applied potential from 0.85 to 2.05 V vs RHE. All difference spectra are generated by subtracting the spectrum measured at OCP from the spectrum measured under applied potentials. (B) Delta absorbance change spectra of the FTO|CoBi at 525 nm as a function of the applied potential (solid black line and squares); CV measurement of FTO|CoBi with a scan rate of 5 mV/s (solid red lines, recorded during SEC measurements). Inset: Steady-state current density measured during SCE, as a function of the absorbance at 525 nm in the SEC difference spectra for FTO|CoBi. (C) Operando UV−vis spectra for different integrated photoanodes at 1.20 V vs RHE under 405 nm monochromatic irradiation. (D) Violet shaded bar: Photocurrent density of the integrated photoanode measured during operando UV−vis spectra. Green shaded bar: calculated current density according to the delta absorbance change spectra of the integrated photoanode corresponding to electrochemical water oxidation current density on CoBi alone.

anode, which was favorable for PEC water oxidation. The normalized open-circuit potential (OCP) decays of the different integrated photoanodes are shown in Figure S6. The slow decay kinetics demonstrated that the BVO|CdS-TPA|CoBi photoanode had long-lived surface holes. These behaviors could contribute to the enhanced performance of PEC water oxidation. A similar trend observed in the time-resolved photoluminescence (TRPL, Figure 3D) further confirmed that the CdS NSs coated on BVO led to a longer carrier lifetime. However, the introduction of TPA led to an obvious decrease in the PL lifetime, indicating the essential role of the TPA in transferring holes efficiently from the BVO to the OEC surface.

Intensity-modulated photocurrent spectroscopy (IMPS) measurements developed by Peter and co-workers[25] were used to further study the effect of the HTs and CdS NSs on interface-charge modulation in the integrated photoanodes in an operational PEC. The IMPS spectra were obtained on different integrated photoanodes to compare the relative rates of charge recombination (k_{rec}) and transfer (k_{trans}) occurring at the BVO/electrolyte interface.[47,48] Figure 4A−E shows typical IMPS responses of BVO|CoBi, BVO|CdS|CoBi, BVO|CdS-CZ|CoBi, BVO|CdS-PTZ|CoBi, and BVO|CdS-TPA|CoBi photoanodes under the applied potential region (0.4−1.2 V vs RHE). Two semicircles in the lower and upper quadrants of the IMPS spectrum correspond to the resistance-capacitance attenuation and the competition between charge transfer and recombination, respectively.[49] The ratio of k_{rec}/k_{trans} was positively proportional to the upper semicircle, and a small value could indicate a faster charge transfer than charge recombination. As shown in Figure 4A,B, the radii of upper semicircles of the BVO|CdS|CoBi photoanodes were smaller than those of the BVO|CoBi photoanodes, indicating that loading of CdS NSs on BVO surfaces retarded charge recombination. After the introduction of HTs into the photoanode, the upper semicircle became further smaller (Figure 4C−E), suggesting that charge recombination was significantly suppressed and charge transfer was significantly accelerated. Moreover, the upper semicircle of the BVO|CdS-HT|CoBi photoanodes became smaller with an increase in the applied potentials. In contrast, the upper semicircle of the BVO|CoBi and BVO|CdS|CoBi photoanodes did not change obviously as applied potentials increased, indicating that rapid charge recombination still existed for the BVO|CoBi and BVO|CdS|CoBi photoanodes under high applied potentials.

In the IMPS technique, the simplified expression for the perturbed photocurrent $j(\omega)$ relating to k_{trans} and k_{rec} is shown in eqs 6 and 7[50,51]

https://doi.org/10.1021/acscatal.2c02773
ACS Catal. 2022, 12, 10028−10038

$$\frac{j_{photo}(\omega)}{j_h(\omega)} = \frac{k_{trans} + i\omega\frac{C}{C_{SC}}}{k_{trans} + k_{rec} + i\omega}\left(\frac{1}{1 + i\omega RC}\right) \quad (6)$$

$$C = \frac{C_{SC}C_H}{C_{SC} + C_H} \quad (7)$$

where $j_h(\omega)$ is the periodic flux of photogenerated holes corresponding to the Gärtner equation, R is the total series resistance, C is the effective capacitance, C_{SC} is the space-charge capacitance, C_H is the Helmholtz capacitance, and ω is the light modulation frequency. Generally, the Helmholtz capacitance is a large space-charge capacitance ($C_{SC} \ll C_H$). According to the generalized theory of IMPS, as the frequency increases, the relaxation in the concentration of the photogenerated hole at the semiconductor surface is characterized by f_{max} (at the apex of the upper semicircle), where $2\pi f_{max} = k_{trans} + k_{rec}$.[25,52] The charge transfer efficiency, in terms of $k_{trans}/(k_{trans} + k_{rec})$, can be derived from the intersections of the semicircle with the real axis at low and high frequencies (i.e., I_1 and I_2, respectively), where $I_1 = I_0k_{trans}/(k_{trans} + k_{rec})$ and $I_2 = I_0C_H/(C_{SC} + C_H)$, as shown in Figure 4F.[47,53] The key parameters k_{rec} and k_{trans} are therefore readily accessible. The values of k_{trans} and k_{rec} for different photoanodes at various potentials are shown in Figure 4G,H. The k_{trans} of BVO|CdS-HT|CoBi surpassed that of BVO|CdS|CoBi and BVO|CoBi at all applied potentials, indicating that the HT greatly promoted the charge transfer kinetics from BVO to CoBi. At higher potentials, the k_{trans} of BVO|CdS-TPA|CoBi was more than 4.8 times that of BVO|CoBi at 1.20 V vs RHE. The k_{rec} of BVO|CoBi remained nearly constant with increasing potentials, and the k_{rec} reduced slightly with an increase in potential for BVO|CdS|CoBi, indicating that the CdS NSs and CoBi could not effectively suppress charge recombination. However, the k_{rec} of BVO|CdS-HT|CoBi reduced obviously, suggesting that HT with superior hole extraction capacity could effectively suppress charge recombination. The value of k_{rec} was suppressed by *a* factor of 2.2−14.2 over the entire potential range after introduction of TPA. At 0.68 V vs RHE (the max point of ABPEs), the value of k_{rec} was 24.3 s^{-1} for BVO|CoBi, which is 6.6 times as large as that of BVO|CdS-TPA|CoBi (3.7 s^{-1}). At higher potentials, this factor increased to 14.2 at 1.20 V vs RHE. These results suggest that charge recombination was markedly suppressed by the introduction of TPA. As shown in Figure 4I, it was noteworthy that BVO|CdS-TPA|CoBi exhibited the highest charge transfer efficiency in a wide range of applied potentials, indicating superior charge separation ability. It was beneficial to PEC water oxidation. These results demonstrated that TPA, serving as the HT, not only accelerated the charge transfer from BVO to CoBi but also reduced surface charge recombination due to rapid lateral hole hopping among adjacent TPA molecules on the BVO surface.[36]

Operando UV−vis spectroelectrochemistry (SEC) was employed to further study the effect of the introduced TPA on oxidation kinetics of Co^{2+} to higher valence states within the CoBi catalyst layer (photograph of the Experimental Setup shown in Figure S7). The characteristic absorptions of different cobalt redox states were first examined. Figure 5A shows delta absorbance changes (ΔAbs) of CoBi on FTO (denoted as FTO|CoBi) as a function of the applied potential from 0.85 to 2.05 V vs RHE with potential steps of every 0.1 V. When the potential increased from 0.85 V up to 1.55 V vs RHE, a broad spectral feature at around 525 nm was visible for FTO|CoBi, which was attributed to the oxidation of Co^{2+} to Co^{3+}.[54,55] The increased absorption corresponds to the additional density of Co^{3+} species within the CoBi layer generated by the applied potential. Figure 5B shows ΔAbs of FTO|CoBi at 525 nm as a function of the applied potential (solid black line and squares) and cyclic voltammetry (CV) measurement (solid red lines, recorded during SEC measurements) of FTO|CoBi with a scan rate of 5 mV/s. Increasing ΔAbs at positively applied potentials was the result of Co^{3+} species accumulation within the CoBi layer. According to Figure 5B, the electrochemical water oxidation current density of FTO|CoBi as a function of ΔAbs at 525 nm is shown in the inset of Figure 5B. The onset of the rising current density for electrocatalytic water oxidation occurred at the applied potential over 1.75 V vs RHE. In contrast, the rise in Co^{3+} absorption with the onset applied potential of 1.45 V vs RHE was way ahead of the start of water oxidation. According to prior reports, the CoBi electrocatalytic water oxidation activity onset behavior as a function of Co^{3+} density was attributed to the requirement for the further oxidation of Co^{3+} to Co^{4+} to enable water oxidation.[55−58] The delayed water oxidation with respect to the conversion of Co^{3+} to Co^{4+} indicated that efficient hole extraction and accumulation to the outer layer of the water oxidation catalyst is of paramount significance.

Operando UV−vis spectra for different integrated photoanodes were recorded at 1.20 V vs RHE under 405 nm monochromatic irradiation, as shown in Figure 5C. Absorbance difference spectra were obtained by subtracting the steady-state absorption spectrum measured without applied potential under dark from the first spectrum measured with an applied potential of 1.20 V vs RHE under 405 nm monochromatic irradiation. ΔAbs of BVO|CoBi (10 mOD) corresponding to the density of Co^{3+} species in the CoBi layer was lower than that of BVO|CdS|CoBi (33 mOD). Surprisingly, ΔAbs increased concomitantly with the photocurrent density when TPA was introduced as HT, indicating that the TPA could accelerate the oxidation of Co^{2+} to Co^{3+} owing to the strong hole extraction capability.

As shown in Figure 5D, the violet shaded bar denotes the photocurrent density of different integrated photoanodes recorded during operando UV−vis spectra. The green shaded bar represents the current of the different integrated photoanode densities calculated according to the spectral delta absorbance changes corresponding to the electrochemical water oxidation current density on CoBi alone. For the BVO|CoBi photoanode, the small ΔAbs (10 mOD) corresponding to the electrochemical water oxidation current density on CoBi was negligible (about 24.1 $\mu A/cm^2$), 1.39% of the observed photocurrent density of BVO|CoBi (1.73 mA/cm^2), as shown in Figure 5D. In other words, the photocurrent of BVO|CoBi was mainly from the direct oxidation of water by the BVO holes, and here, the main role of CoBi was to passivate the surface of BVO, resulting in the low OER activity. For the BVO|CdS|CoBi photoanode, the ΔAbs (33 mOD) was higher than that of BVO|CoBi, which was attributed to the CdS NSs promoting hole transfer to CoBi. However, the corresponding electrochemical water oxidation current density on CoBi was only 0.52 mA/cm^2, 22.1% of the observed photocurrent density of BVO|CdS|CoBi (2.36 mA/cm^2), as shown in Figure 5D. However, for the BVO|CdS-TPA|CoBi photoanode, the ΔAbs (52 mOD) corresponding electrochemical water oxidation current density on CoBi was about 4.45 mA/cm^2,

https://doi.org/10.1021/acscatal.2c02773
ACS Catal. 2022, 12, 10028−10038

almost identical to the photocurrent density of BVO|CdS-TPA|CoBi (4.56 mA/cm^2). In other words, the photocurrent density of BVO|CdS-TPA|CoBi was mainly from the CoBi catalytic water oxidation instead of BVO holes, resulting in excellent PEC performance. We believe that the TPA with strong hole extraction capability promoted hole transfer from BVO to CoBi and accelerated the kinetics of oxidation of Co^{2+} to Co^{3+}. Efficient hole extraction and retarded charge recombination help accumulate a much higher concentration of Co^{3+} species within the CoBi layer. The collective results indicate that the effective interface-charge modulation PEC system with TPA anchored onto CdS NSs is a feasible strategy to achieve efficient charge separation for boosting PEC water splitting.

CONCLUSIONS

A novel photoelectrochemical water-splitting cell was constructed where the photoanode utilized a cascade band alignment configuration for efficient photoinduced hole transfer to the water oxidation catalyst. The cascade band alignment of BVO, CdS, surface-anchored HT, and OEC helped transfer the photogenerated holes from BVO to OEC in microseconds while retarding unwanted charge recombination to milliseconds. The greatly increased disparity in the two competing kinetic processes contributed to the highest photocurrent density of 5.2 mA/cm^2 at 1.23 V (vs RHE) for water oxidation, which was a remarkable 6-fold increase compared with the pristine BVO photoanode. Furthermore, the oxygen evolution center of the best-performing photoanode BVO|CdS-TPA|CoBi was shown to be on CoBi other than the literature-reported BVO surface because of rapid hole transfer and accumulation outcompeting unwanted charge recombination. Our findings provide a promising avenue for constructing integrated photoanodes for highly efficient BVO-based PEC water-splitting devices.

ASSOCIATED CONTENT

Supporting Information

The Supporting Information is available free of charge at https://pubs.acs.org/doi/10.1021/acscatal.2c02773.

Experimental procedures for the synthesis of the different $BiVO_4$-based photoanodes; calculation of the surface coverages of HTs on BVO|CdS; UV−vis diffuse reflectance spectra of different photoanodes; electrochemical and photoelectrochemical methods; faradic efficiency determination; IMPS and ABPE measurements; nanosecond transient absorption (TA) spectroscopy and operando UV−vis spectroscopy measurements; and experimental procedures for the synthesis and ^{1}H and ^{13}C NMR spectra of relevant molecules (PDF)

AUTHOR INFORMATION

Corresponding Author

Ke Hu − *Department of Chemistry, Fudan University, Shanghai 200433, P. R. China;* orcid.org/0000-0002-0240-7192; Email: khu@fudan.edu.cn

Authors

Fushuang Niu − *Department of Chemistry, Fudan University, Shanghai 200433, P. R. China*

Quan Zhou − *School of Advanced Study, Taizhou University, Jiaojiang, Zhejiang 318000, P. R. China*

Yiming Han − *Department of Chemistry, Fudan University, Shanghai 200433, P. R. China*

Rong Liu − *Department of Chemistry, Fudan University, Shanghai 200433, P. R. China*

Zijian Zhao − *Department of Chemistry, Fudan University, Shanghai 200433, P. R. China*

Zhenghao Zhang − *Department of Chemistry, Fudan University, Shanghai 200433, P. R. China*

Complete contact information is available at: https://pubs.acs.org/10.1021/acscatal.2c02773

Notes

The authors declare no competing financial interest.

ACKNOWLEDGMENTS

This work was sponsored by the National Natural Science Foundation of China (21872037 and 22173022) and the Natural Science Foundation of Shanghai (21ZR1404400).

REFERENCES

(1) Zhang, X.; Zhai, P.; Zhang, Y.; Wu, Y.; Wang, C.; Ran, L.; Gao, J.; Li, Z.; Zhang, B.; Fan, Z.; et al. Engineering Single-Atomic Ni-N_4-O Sites on Semiconductor Photoanodes for High-Performance Photoelectrochemical Water Splitting. *J. Am. Chem. Soc.* **2021**, *143*, 20657−20669.

(2) Ning, X.; Lu, B.; Zhang, Z.; Du, P.; Ren, H.; Shan, D.; Chen, J.; Gao, Y.; Lu, X. An Efficient Strategy for Boosting Photogenerated Charge Separation by Using Porphyrins as Interfacial Charge Mediators. *Angew. Chem., Int. Ed.* **2019**, *58*, 16800−16805.

(3) Zachäus, C.; Abdi, F. F.; Peter, L. M.; Van De Krol, R. J. C. s. Photocurrent of $BiVO_4$ is limited by surface recombination, not surface catalysis. *Chem. Sci.* **2017**, *8*, 3712−3719.

(4) Wang, S.; Wang, X.; Liu, B.; Guo, Z.; Ostrikov, K.; Wang, L.; Huang, W. Vacancy defect engineering of $BiVO_4$ photoanodes for photoelectrochemical water splitting. *Nanoscale* **2021**, *13*, 17989−18009.

(5) Zhang, K.; Jin, B.; Park, C.; Cho, Y.; Song, X.; Shi, X.; Zhang, S.; Kim, W.; Zeng, H.; Park, J. H. Black phosphorene as a hole extraction layer boosting solar water splitting of oxygen evolution catalysts. *Nat. Commun.* **2019**, *10*, No. 2001.

(6) Fang, G.; Liu, Z.; Han, C. J. A. S. S. Enhancing the PEC water splitting performance of $BiVO_4$ co-modifying with NiFeOOH and Co-Pi double layer cocatalysts. *Appl. Surf. Sci.* **2020**, *515*, No. 146095.

(7) Wang, S.; Chen, P.; Bai, Y.; Yun, J. H.; Liu, G.; Wang, L. J. A. M. New $BiVO_4$ Dual Photoanodes with Enriched Oxygen Vacancies for Efficient Solar-Driven Water Splitting. *Adv. Mater.* **2018**, *30*, No. 1800486.

(8) Chen, H.; Li, J.; Yang, W.; Balaghi, S. E.; Triana, C. A.; Mavrokefalos, C. K.; Patzke, G. R. The Role of Surface States on Reduced TiO_2@$BiVO_4$ Photoanodes: Enhanced Water Oxidation Performance through Improved Charge Transfer. *ACS Catal.* **2021**, *11*, 7637−7646.

(9) Li, L.; Li, J.; Bai, J.; Zeng, Q.; Xia, L.; Zhang, Y.; Chen, S.; Xu, Q.; Zhou, B. J. N. Serial hole transfer layers for a $BiVO_4$ photoanode with enhanced photoelectrochemical water splitting. *Nanoscale* **2018**, *10*, 18378−18386.

(10) Wang, S.; Wang, X.; Liu, B.; Guo, Z.; Ostrikov, K.; Wang, L.; Huang, W. Vacancy defect engineering of $BiVO_4$ photoanodes for photoelectrochemical water splitting. *Nanoscale* **2021**, *13*, 17989−18009.

(11) Yang, J. W.; Park, I. J.; Lee, S. A.; Lee, M. G.; Lee, T. H.; Park, H.; Kim, C.; Park, J.; Moon, J.; Kim, J. Y.; Jang, H. W. Near-complete charge separation in tailored $BiVO_4$-based heterostructure photoanodes toward artificial leaf. *Appl. Catal., B* **2021**, *293*, No. 120217.

(12) Luo, W.; Li, Z.; Yu, T.; Zou, Z. Effects of surface electrochemical pretreatment on the photoelectrochemical performance of Mo-doped $BiVO_4$. *J. Phys. Chem. C* **2012**, *116*, 5076−5081.
(13) Wang, M.; Guo, P.; Chai, T.; Xie, Y.; Han, J.; You, M.; Wang, Y.; Zhu, T. J. Compounds. Effects of Cu dopants on the structures and photocatalytic performance of cocoon-like Cu-$BiVO_4$ prepared via ethylene glycol solvothermal method. *J. Alloys Compd.* **2017**, *691*, 8−14.
(14) Sarker, H. P.; Rao, P. M.; Huda, M. N. J. C. Niobium Doping in $BiVO_4$: Interplay Between Effective Mass, Stability, and Pressure. *ChemPhysChem* **2019**, *20*, 773−784.
(15) Österbacka, N.; Wiktor, J. Influence of Oxygen Vacancies on the Structure of $BiVO_4$. *J. Phys. Chem. C* **2021**, *125*, 1200−1207.
(16) Zhang, J.; Nosaka, Y. Generation of OH radicals and oxidation mechanism in photocatalysis of WO_3 and $BiVO_4$ powders. *J. Photochem. Photobiol., A* **2015**, *303*−*304*, 53−58.
(17) Wang, S.; Chen, P.; Yun, J. H.; Hu, Y.; Wang, L. J. A. C. An electrochemically treated $BiVO_4$ photoanode for efficient photoelectrochemical water splitting. *Angew. Chem.* **2017**, *129*, 8620−8624.
(18) Zhong, D. K.; Choi, S.; Gamelin, D. R. Near-complete suppression of surface recombination in solar photoelectrolysis by "Co-Pi" catalyst-modified W: $BiVO_4$. *J. Am. Chem. Soc.* **2011**, *133*, 18370−18377.
(19) Pan, J. B.; Wang, B. H.; Wang, J. B.; Ding, H. Z.; Zhou, W.; Liu, X.; Zhang, J. R.; Shen, S.; Guo, J. K.; Chen, L. J. A. C.; et al. Activity and Stability Boosting of an Oxygen-Vacancy-Rich $BiVO_4$ Photoanode by NiFe-MOFs Thin Layer for Water Oxidation. *Angew. Chem.* **2021**, *133*, 1453−1460.
(20) Wang, Q.; Niu, T.; Wang, L.; Huang, J.; She, H. NiFe layered double-hydroxide nanoparticles for efficiently enhancing performance of $BiVO_4$ photoanode in photoelectrochemical water splitting. *Chin. J. Catal.* **2018**, *39*, 613−618.
(21) Li, Y.; Wang, Q.; Hu, X.; Meng, Y.; She, H.; Wang, L.; Huang, J.; Zhu, G. Constructing NiFe-metal-organic frameworks from NiFe-layered double hydroxide as a highly efficient cocatalyst for $BiVO_4$ photoanode PEC water splitting. *Chem. Eng. J.* **2021**, No. 133592.
(22) Mohanta, M. K.; Sahu, T. K.; Gogoi, D.; Peela, N. R.; Qureshi, M. Hexagonal Boron Nitride Quantum Dots as a Superior Hole Extractor for Efficient Charge Separation in WO_3-Based Photoelectrochemical Water Oxidation. *ACS Appl. Energy Mater.* **2019**, *2*, 7457−7466.
(23) Qin, Q.; Cai, Q.; Hong, W.; Jian, C.; Liu, W. Improved hole extraction and durability of $BiVO_4$ photoanode for solar water splitting under extreme pH condition. *Chem. Eng. J.* **2020**, *402*, No. 126227.
(24) Tang, Y.; Wang, R.; Yang, Y.; Yan, D.; Xiang, X. Highly Enhanced Photoelectrochemical Water Oxidation Efficiency Based on Triadic Quantum Dot/Layered Double Hydroxide/$BiVO_4$ Photoanodes. *ACS Appl. Mater. Interfaces* **2016**, *8*, 19446−19455.
(25) Zachäus, C.; Abdi, F. F.; Peter, L. M.; van de Krol, R. Photocurrent of $BiVO_4$ is limited by surface recombination, not surface catalysis. *Chem. Sci.* **2017**, *8*, 3712−3719.
(26) Alam, S.; Qureshi, M. Interfacial Bridging Strategy for Charge Extraction/Injection in the $BiVO_4$/CoSn-Layered Double Hydroxide p−n Heterojunction Approach Using Graphene Quantum Dots for Enhanced Water Oxidation Kinetics. *J. Phys. Chem. Lett.* **2021**, *12*, 8947−8955.
(27) Zeng, G.; Deng, Y.; Yu, X.; Zhu, Y.; Fu, X.; Zhang, Y. Ultrathin g-C_3N_4 as a hole extraction layer to boost sunlight-driven water oxidation of $BiVO_4$-Based photoanode. *J. Power Sources* **2021**, *494*, No. 229701.
(28) Zhao, M.; Chen, T.; He, B.; Hu, X.; Huang, J.; Yi, P.; Wang, Y.; Chen, Y.; Li, Z.; Liu, X. Photothermal effect-enhanced photoelectrochemical water splitting of a $BiVO_4$ photoanode modified with dual-functional polyaniline. *J. Mater. Chem. A* **2020**, *8*, 15976−15983.
(29) Pan, Q.; Chen, T.; Ma, L.; Wang, G.; Hu, W.-B.; Zou, Z.; Wen, K.; Yang, H. Covalent Triazine-Based Polymers with Controllable Band Alignment Matched with $BiVO_4$ To Boost Photogeneration of Holes for Water Splitting. *Chem. Mater.* **2019**, *31*, 8062−8068.
(30) Hu, K.; Meyer, G. J. Lateral Intermolecular Self-Exchange Reactions for Hole and Energy Transport on Mesoporous Metal Oxide Thin Films. *Langmuir* **2015**, *31*, 11164−11178.
(31) Gao, L.; Schloemer, T. H.; Zhang, F.; Chen, X.; Xiao, C.; Zhu, K.; Sellinger, A. Carbazole-Based Hole-Transport Materials for High-Efficiency and Stable Perovskite Solar Cells. *ACS Appl. Energy Mater.* **2020**, *3*, 4492−4498.
(32) Liu, J.; Liu, W.; Aydin, E.; Harrison, G. T.; Isikgor, F. H.; Yang, X.; Subbiah, A. S.; De Wolf, S. Lewis-Acid Doping of Triphenylamine-Based Hole Transport Materials Improves the Performance and Stability of Perovskite Solar Cells. *ACS Appl. Mater. Interfaces* **2020**, *12*, 23874−23884.
(33) Zhang, J.; Xu, B.; Yang, L.; Ruan, C.; Wang, L.; Liu, P.; Zhang, W.; Vlachopoulos, N.; Kloo, L.; Boschloo, G.; et al. The Importance of Pendant Groups on Triphenylamine-Based Hole Transport Materials for Obtaining Perovskite Solar Cells with over 20% Efficiency. *Adv. Energy Mater.* **2018**, *8*, No. 1701209.
(34) Zhang, F.; Wang, S.; Zhu, H.; Liu, X.; Liu, H.; Li, X.; Xiao, Y.; Zakeeruddin, S. M.; Grätzel, M. Impact of Peripheral Groups on Phenothiazine-Based Hole-Transporting Materials for Perovskite Solar Cells. *ACS Energy Lett.* **2018**, *3*, 1145−1152.
(35) Ding, X.; Wang, H.; Chen, C.; Li, H.; Tian, Y.; Li, Q.; Wu, C.; Ding, L.; Yang, X.; Cheng, M. Passivation functionalized phenothiazine-based hole transport material for highly efficient perovskite solar cell with efficiency exceeding 22%. *Chem. Eng. J.* **2021**, *410*, No. 128328.
(36) Wang, D.; Xu, Z.; Sheridan, M. V.; Concepcion, J. J.; Li, F.; Lian, T.; Meyer, T. J. Photodriven water oxidation initiated by a surface bound chromophore-donor-catalyst assembly. *Chem. Sci.* **2021**, *12*, 14441−14450.
(37) Niu, F.; Zhou, Q.; Liu, R.; Hu, K. Photoinduced Hole Hopping across CdS Quantum Dot Surfaces for Photoelectrochemical Water Oxidation. *ACS Appl. Energy Mater.* **2022**, *5*, 1244−1251.
(38) Jian, J.; Xu, Y.; Yang, X.; Liu, W.; Fu, M.; Yu, H.; Xu, F.; Feng, F.; Jia, L.; Friedrich, D.; et al. Embedding laser generated nanocrystals in $BiVO_4$ photoanode for efficient photoelectrochemical water splitting. *Nat. Commun.* **2019**, *10*, No. 2609.
(39) Kim, J. H.; Lee, J. S. Elaborately Modified $BiVO_4$ Photoanodes for Solar Water Splitting. *Adv. Mater.* **2019**, *31*, No. 1806938.
(40) Ren, S.; Sun, M.; Guo, X.; Liu, X.; Zhang, X.; Wang, L. Interface-Confined Surface Engineering via Photoelectrochemical Etching toward Solar Neutral Water Splitting. *ACS Catal.* **2022**, *12*, 1686−1696.
(41) Pareek, A.; Paik, P.; Borse, P. H. J. L. Nanoniobia modification of CdS photoanode for an efficient and stable photoelectrochemical cell. *Langmuir* **2014**, *30*, 15540−15549.
(42) Kafizas, A.; Xing, X.; Selim, S.; Mesa, C. A.; Ma, Y.; Burgess, C.; McLachlan, M. A.; Durrant, J. R. J. C. T. Ultra-thin Al_2O_3 coatings on $BiVO_4$ photoanodes: Impact on performance and charge carrier dynamics. *Catal. Today* **2019**, *321*−*322*, 59−66.
(43) Lindsey, C. P.; Patterson, G. D. Detailed comparison of the Williams–Watts and Cole–Davidson functions. *J. Chem. Phys.* **1980**, *73*, 3348−3357.
(44) Xia, L.; Li, J.; Bai, J.; Li, L.; Chen, S.; Zhou, B. $BiVO_4$ Photoanode with Exposed (040) Facets for Enhanced Photoelectrochemical Performance. *Nano-Micro Lett.* **2018**, *10*, No. 11.
(45) Kahraman, A.; Vishlaghi, M. B.; Baylam, I.; Ogasawara, H.; Sennaroğlu, A.; Kaya, S. The Fast-Track Water Oxidation Channel on $BiVO_4$ Opened by Nitrogen Treatment. *J. Phys. Chem. Lett.* **2020**, *11*, 8758−8764.
(46) Li, L.; Li, J.; Bai, J.; Zeng, Q.; Xia, L.; Zhang, Y.; Chen, S.; Xu, Q.; Zhou, B. Serial hole transfer layers for a $BiVO_4$ photoanode with enhanced photoelectrochemical water splitting. *Nanoscale* **2018**, *10*, 18378−18386.
(47) Zhou, D.; Fan, K.; Zhuo, Q.; Zhao, Y.; Sun, L. In Situ Induced Crystalline−Amorphous Heterophase Junction by K^+ to Improve Photoelectrochemical Water Oxidation of $BiVO_4$. *ACS Appl. Mater. Interfaces* **2021**, *13*, 2723−2733.

(48) Yu, F.; Li, F.; Yao, T.; Du, J.; Liang, Y.; Wang, Y.; Han, H.; Sun, L. Fabrication and Kinetic Study of a Ferrihydrite-Modified $BiVO_4$ Photoanode. *ACS Catal.* **2017**, *7*, 1868−1874.
(49) Xie, J.; Guo, C.; Yang, P.; Wang, X.; Liu, D.; Li, C. M. Bifunctional ferroelectric $BiFeO_3$ passivated $BiVO_4$ photoanode for efficient and stable solar water oxidation. *Nano Energy* **2017**, *31*, 28−36.
(50) Kandiel, T. A.; Ahmed, M. G.; Ahmed, A. Y. Physical Insights into Band Bending in Pristine and Co-Pi-Modified $BiVO_4$ Photoanodes with Dramatically Enhanced Solar Water Splitting Efficiency. *J. Phys. Chem. Lett.* **2020**, *11*, 5015−5020.
(51) Cardenas-Morcoso, D.; Bou, A.; Ravishankar, S.; García-Tecedor, M.; Gimenez, S.; Bisquert, J. Intensity-Modulated Photocurrent Spectroscopy for Solar Energy Conversion Devices: What Does a Negative Value Mean? *ACS Energy Lett.* **2020**, *5*, 187−191.
(52) Peat, R.; Peter, L. M. A study of the passive film on iron by intensity modulated photocurrent spectroscopy. *J. Electroanal. Chem. Interfacial Electrochem.* **1987**, *228*, 351−364.
(53) Meng, Q.; Zhang, B.; Yang, H.; Liu, C.; Li, Y.; Kravchenko, A.; Sheng, X.; Fan, L.; Li, F.; Sun, L. Remarkable synergy of borate and interfacial hole transporter on $BiVO_4$ photoanodes for photoelectrochemical water oxidation. *Mater. Adv.* **2021**, *2*, 4323−4332.
(54) Lee, S.; Moysiadou, A.; Chu, Y.-C.; Chen, H. M.; Hu, X. Tracking high-valent surface iron species in the oxygen evolution reaction on cobalt iron (oxy)hydroxides. *Energy Environ. Sci.* **2022**, *15*, 206−214.
(55) Ma, Y.; Kafizas, A.; Pendlebury, S. R.; Le Formal, F.; Durrant, J. R. Photoinduced absorption spectroscopy of CoPi on $BiVO_4$: the function of CoPi during water oxidation. *Adv. Funct. Mater.* **2016**, *26*, 4951−4960.
(56) Surendranath, Y.; Kanan, M. W.; Nocera, D. Mechanistic studies of the oxygen evolution reaction by a cobalt-phosphate catalyst at neutral pH. *J. Am. Chem. Soc.* **2010**, *132*, 16501−16509.
(57) Ahn, H. S.; Bard, A. J. Surface interrogation of CoPi water oxidation catalyst by scanning electrochemical microscopy. *J. Am. Chem. Soc.* **2015**, *137*, 612−615.
(58) McAlpin, J. G.; Surendranath, Y.; Dinca, M.; Stich, T. A.; Stoian, S. A.; Casey, W. H.; Nocera, D. G.; Britt, R. D. EPR evidence for Co (IV) species produced during water oxidation at neutral pH. *J. Am. Chem. Soc.* **2010**, *132*, 6882−6883.

https://doi.org/10.1021/acscatal.2c02773
ACS Catal. 2022, 12, 10028−10038